Experimental determination of solute redistribution behavior during solidification of additively manufactured 316L

Sylvain Dépinoy, Mohamed Sennour, Lyliat Ferhat, Christophe Colin

Version of Record: https://www.sciencedirect.com/science/article/pii/S1359646220307855
Manuscript_23fd9e02690c26a303dff4a0a83bbe5f

Experimental determination of solute redistribution behavior during solidification of additively manufactured 316L

Sylvain Dépinoy, Mohamed Sennour, Lyliat Ferhat, Christophe Colin*

MINES ParisTech, PSL University, MAT - Centre des Matériaux, CNRS UMR 7633, BP 87, 91003 Evry, France

*Corresponding author: sylvain.depinoy@mines-paristech.fr

Graphical abstract

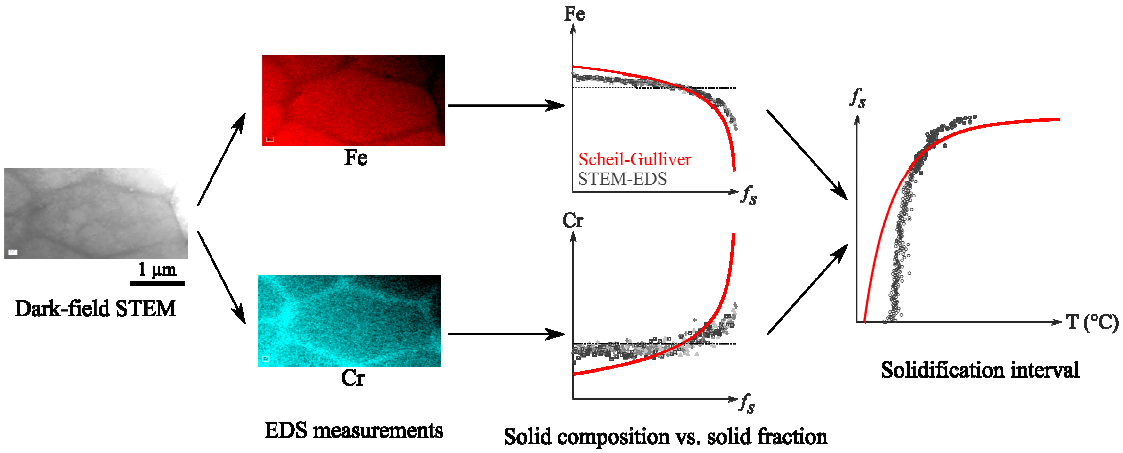

Abstract

Chemical measurement points obtained with energy dispersive X-ray spectroscopy (EDS) in scanning transmission electron microscopy (STEM) were processed by a modified weighted interval rank sort (WIRS) method in order to study the solute redistribution during solidification of an additively manufactured 316L stainless steel. Scheil-Gulliver calculations give a good first approximation, although the extent of segregation is lower experimentally than theoretically. These discrepancies are believed to be due to the fast solidification rate involved. STEM-EDS data processed by the modified WIRS method is a strong and reliable technique for characterizing the segregation profile for additively manufactured metals, and the proposed method is shown to reduce the experimental uncertainty associated with the quantification of minor elements.

Keywords: additive manufacturing, solidification microstructure, segregation, energy dispersive X-ray spectroscopy (EDXS)

Solute redistribution occurs during solidification of metallic alloys due to differences in solubility in liquid and solid phases. As a result, local gradients of chemical composition between the first solid germs (the dendrite core) and the last drops of liquid (interdendritic regions) can be observed in fully solidified materials. Owing to the fast solidification rates involved, metallic alloys elaborated by additive manufacturing tend to exhibit very fine dendritic or cellular intragranular substructures and thus very localized composition gradients [1,2]. Depending on the material, these chemical heterogeneities can have a beneficial or a detrimental influence on the final properties. For instance, the molybdenum enrichment of the intercellular regions in 316L is thought to reduce the corrosion resistance [3] but may improve the mechanical properties [4]. Solute redistribution also lead to the precipitation of brittle intermetallic and chains of Laves phases in Inconel 718 [5], to a large amount of retained austenite in martensitic steels [6,7] and, in conjunction with high thermal stresses, to solidification cracking in Inconel 738 [8]. Finally, solute redistribution enables a fine eutectic structure in Al-12Si alloys, leading to better mechanical properties that can then be tailored by an appropriate heat treatment [9]. Despite all these effects, no experimental studies are dedicated to the investigation of solute redistribution during additive manufacturing. Reported experimental assessments are either qualitative or semi-quantitative, i.e. elemental mapping or line-scans using energy dispersive X-ray spectroscopy (EDS) in scanning transmission electron microscopy (STEM) [1,2,9–11]. In this work, STEM-EDS measurement points are processed by a modified weighted interval rank sort (WIRS) method to quantitatively reconstruct the microsegregation behavior of a 316L stainless steel elaborated by Laser Powder Bed Fusion (L-PBF). The evolution of the solid composition as a function of the solid fraction, the tendency of elements to segregate and the solidification interval are compared to theoretical Scheil-Gulliver calculations performed with Thermo-Calc.

A 20×30×13 mm^3 316L specimen was built on a Concept Laser M2 machine using a laser power P = 120 W, a scanning speed v = 30 mm/s, a laser spot size φ = 200 µm, a slicing thickness of 50 µm and a hatch spacing of 198 µm, i.e. an overlap of 33% between adjacent tracks. Such process parameters are not representative of industrial practices: as a reference, common process parameters

for 316L stainless steel are P between 180 W and 370 W, v between 700 mm/s to 800 mm/s, φ between 100 µm and 140 µm and a hatch spacing between 95 µm and 115 µm, resulting in a minimum cooling rate of 10^6 °C/s and a typical cell diameter of 0.5 µm [12]. The parameters used in this study were chosen as they induce a slower cooling rate, and thus bigger solidification cells. Solid-state diffusion after solidification can occur due to localize re-heating, for instance the melting of neighboring laser tracks or subsequent layers. Larger cells reduce the extent of solid-state diffusion by increasing the length over which elements have to diffuse and by decreasing local gradients of chemical potential, and thus the diffusion speed. Furthermore, a specific scanning strategy was designed to minimize this amount of re-heating. For a given layer, every four laser tracks were first melted, then the adjacent laser tracks, and so on. Such strategy allowed each laser track to cool down for approximately 30 seconds before being partially re-melted by its neighbor. A unidirectional scanning strategy was used with no rotation between layers. Finally, an interlayer time of 60 s was applied to reduce the heat accumulation in the already built layers [13].

The TEM thin foil was prepared as follows. A 200 µm thick disk was cut close to the top surface of a 3 mm diameter cylinder machined following the building direction, grinded down to a thickness of 100 µm, then electrolytically thinned using a 45% butoxyethanol, 45% acetic acid, 10% perchloric acid solution with a 40 V tension at 0 °C. Plasma cleaning for 120 seconds was performed just before observation on the TEM. STEM observations were conducted on a FEI Tecnai F20 FEG-TEM with a 200 kV acceleration voltage. Three areas hereafter referred to as areas “1” to “3” were selected for EDS analyses (Figure 1a), all belonging to a single <110> austenite grain aligned with the building direction. The observed microstructure consists of elongated solidification cells (light grey areas) separated by segregated zones (dark grey areas) and dislocations walls (Figure 1b). Dislocation cells embedded in the solidification cells can be observed (Figure 1b), in good agreement with the observations reported by Bertsch et al for a similar cooling rate [14], showing that no recovery or recrystallization occurred in the material during the elaboration. Several authors have shown that the <110> orientation in 316L stainless steel built by L-PBF stems from the growth of solidification cells along a <001> direction inclined with a 45° angle with respect to the building direction [15,16]. Thus,

cylindrical cells belonging to a <110> grain observed in the plane perpendicular to the building direction should appear as ellipsoids with an aspect ratio of $1/\cos(\pi/4) \sim 1.41$, close to the average aspect ratio of 1.57 measured in Figure 1a. The average diameter of the cells was thus deduced to be about 1.2 µm, corresponding to a cooling rate in the order of 3×10^5 °C/s [17]. Finally, small precipitates were sometimes found at the segregated zones but were not characterized. Several authors identified similar nano-inclusions as oxides containing Mn, Cr and Si [2,4,11,18].

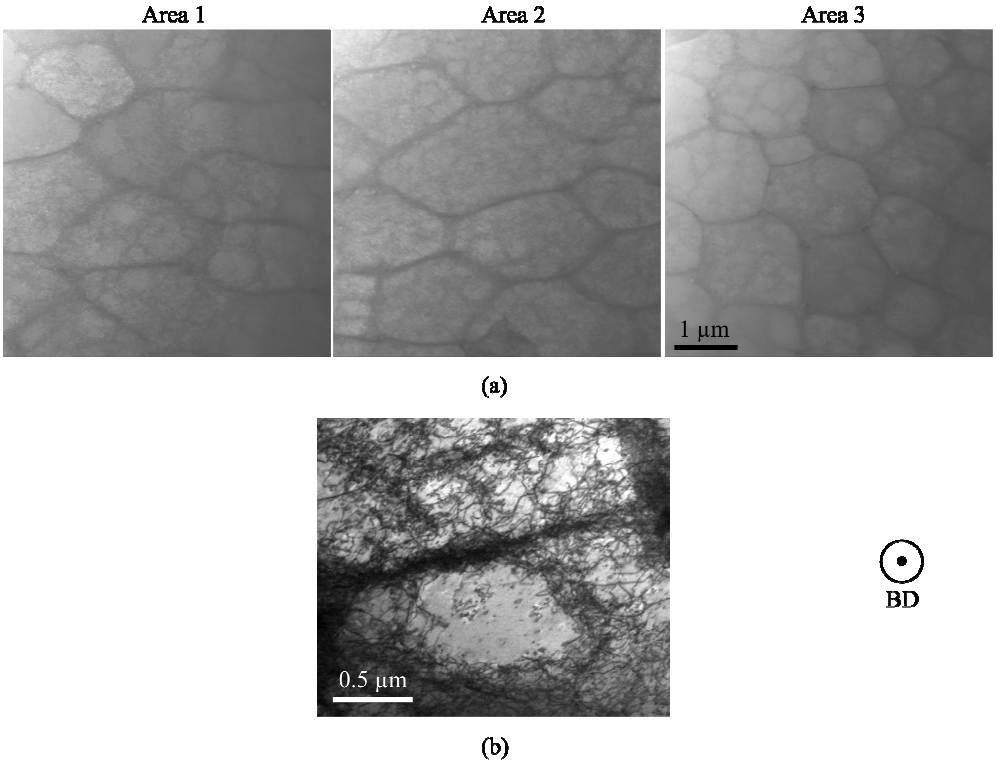

Figure 1: *(a) Dark-field STEM observations of the three areas selected for EDS analyses and (b) Bright-field STEM close-up view of the intercellular region showing dislocation embedded in solidification cells. Observations were performed close to the [110] zone axis.*

EDS analyses were performed using a Bruker XFlash 6T | 60 detector, with an α-tilt of the specimen holder close or equal to +20° to improve the counting rate and a counting time of 30 seconds. 320 measurement points were performed, respectively 100 (10x10 grid), 121 (11x11 grid) and 99 (11x9 grid) for areas 1, 2 and 3. Measurement point spacing was kept constant at 500 nm. Spectra were processed with the Esprit 2.2 software: quantification of Si, Cr, Mn, Fe and Ni elements was performed based on their K lines, and Mo using its L line. A constant carbon composition of 0.02

wt% was assumed for all points. Quantification was conducted using the Cliff-Lorimer method with calculated k-factors corresponding to a sample density and thickness of 8 g/cm^3 and 100 nm, respectively. The uneven thickness of the measured areas, highlighted by the gradient of luminosity in Figure 1, has no significant effect on the quantification: k-factors calculated for a thickness of 50 nm yielded a similar quantification, with relative deviations of about 7%, 1%, 0.2%, 0.1%, 0.7% and 4% for Si, Cr, Mn, Fe, Ni and Mo, respectively. Four measurements points were discarded as they showed unrealistically high levels of manganese. Table 1 summarizes the quantification results for the three areas as well as the nominal powder composition. A relative deviation of about 10% was obtained for minor elements (i.e. Mn, Si and Mo) between the different areas, but an overall good agreement was reached between EDS quantifications of the different areas and the powder composition.

	C	Si	Cr	Mn	Fe	Ni	Mo
Powder composition	0.02	0.65	17.9	1.40	bal.	12.8	2.40
EDS (Area 1)	0.02*	0.61	17.2	1.57	bal.	12.7	3.02
EDS (Area 2)	0.02*	0.56	17.6	1.43	bal.	12.8	2.76
EDS (Area 3)	0.02*	0.64	17.3	1.38	bal.	12.8	3.25
EDS (average)	0.02*	0.60	17.4	1.46	bal.	12.8	2.99

Table 1*: Nominal composition and average of EDS measurements (in wt%). Powder composition was determined by XRF spectroscopy, combustion analysis and loss on drying by the supplier (Concept Laser). Asterisks indicate imposed concentrations.*

Measurements data was processed using the weighted interval rank sort (WIRS) method [19] which allows to reconstruct the evolution of the solid composition C_s as a function of the solid fraction f_s. The WIRS method was modified as follows: instead of considering the absolute concentration C_i^j of an element *j* at the EDS point location *i*, the nondimensional concentration $C_i^{*j} = C_i^j / C_{0,k}^j$ was used, were $C_{0,k}^j$ denotes the average concentration of *j* in area *k*. Such modification allows to process together datasets with similar trends but different absolute values, providing that each dataset is representative of the investigated system, as can happen for instance in the case of areas of slightly difference thickness. The nondimensional weighted value $\bar{C}_i^{*j}$ is given by $\bar{C}_i^{*j} = \left(C_i^{*j} - C_{min}^{*j}\right) / \sigma^{*j}$ for elements which segregate to the liquid and $\bar{C}_i^{*j} = \left(C_{max}^{*j} - C_i^{*j}\right) / \sigma^{*j}$ for elements that partition to the solid, where C_{min}^{*j} and C_{max}^{*j} are respectively the minimum and the maximum nondimensional

concentration of that element in the dataset and σ^{*j} the relative uncertainty of the measurement. The corresponding solid fraction $f_s(i)$ is given by $f_s(i) = (R_i - 0.5)/\,N$, where R_i is the rank number of the measurement based on the sorted average of the weighted values for all measurements in ascending order, and *N* is the total number of measurements. The tendency of an element to segregate is defined by its partition coefficient $k^j = C_s^{*j}/C_l^{*j}$, where C_l^* is the nondimensional liquid composition. The evolution of *k* with the solid fraction was determined by the mass balance analysis (MBA) method [20], such that $k^j(f_s) = \left[C_s^{*j}(f_s)(1-f_s)\right]/\left[1 - \int_0^{f_s} C_s^{*j}(f_s)\, df_s\right]$. Solid fractions close to 1 lead to large uncertainties of *k* [20], thus partition coefficients were determined for f_s up to 0.95. Si was not taken into account in the weighting algorithm: its low mean concentration implies that very small variations of C_i^{*Si} leads to large values of $\bar{C}_i^{*Si}$, giving this element a disproportionate influence on the rank determination.

Experimental data were compared to Scheil-Gulliver calculations performed with Thermo-Calc version 2020a using the TCFE9 database and the nominal powder composition. Only liquid and austenite phases were considered in the calculations since no ferrite was observed experimentally. In the following, *k* coefficients obtained with Thermo-Calc are referred to by k_e as they correspond to partition coefficients at equilibrium. Complementary calculations accounting for backdiffusion, using a cooling rate of 10^5 °C/s, showed that diffusion in the solid phase during solidification was negligible. The effect of solid-state diffusion on the composition profile was assessed with Dictra using the MOBFE4 database and the Scheil-Gulliver composition over a length of 0.6 µm (i.e. half the average cell size), assuming a cylindrical closed system. Diffusion calculations were performed at 1000°C for 1 second, an arbitrarily but highly unrealistic time: as a mean of comparison, the laser takes 0.007 seconds to advance a length corresponding to its diameter. Solidification interval was determined with Thermo-Calc for three different solid compositions C_s^j corresponding to (i) experimental data points using their solid fraction as determined by the modified WIRS method, (ii) Scheil-Gulliver calculations performed with Thermo-Calc (theoretical Scheil-Gulliver), and (iii) Scheil-Gulliver equation such that $C_s^j = k^j C_{0,nom}(1-f_s)^{k^j-1}$, where $C_{0,nom}$ is the nominal powder composition and

k^j the mean value of the partition coefficient determined by the MBA method (experimental Scheil-Gulliver). This last case corresponds to $C_s^j = C_{0,nom} \times C_s^{*j}$, in other words it extrapolates the variations in solute concentrations as measured by STEM-EDS to the nominal composition of the material. This allows a direct comparison with the theoretical Scheil-Gulliver.

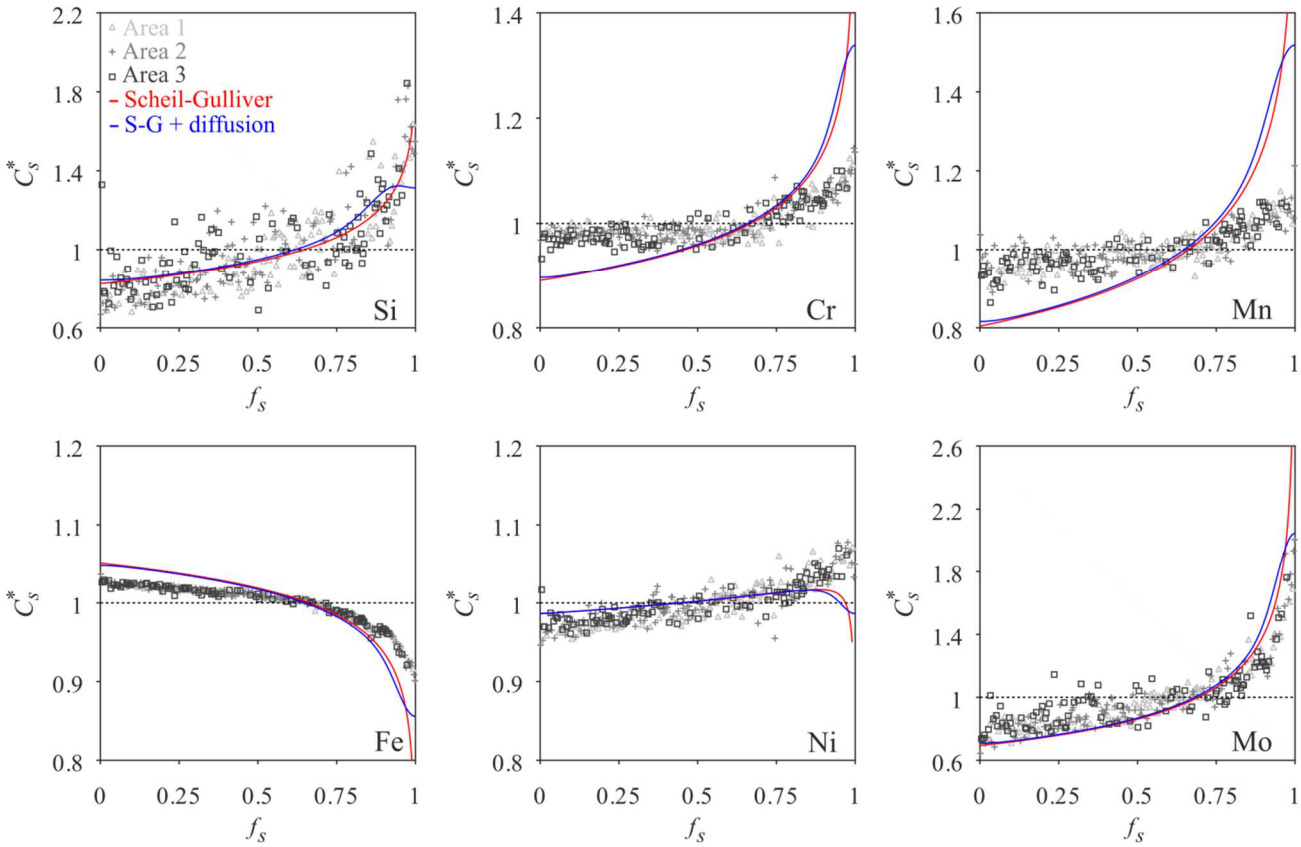

Figure 2: *Comparison between the evolution of the nondimensional solid composition as a function of the solid fraction determined by STEM-EDS and calculated using Thermo-Calc and Dictra. The x-axis for the diffusion calculations corresponds to x/r, where x is the distance from the cell core and r is the mean radius of the solidification cells, such that it is equivalent to f_s.*

Figures 2, 3 and 4 show the comparison between the experimental measurements and theoretical Scheil-Gulliver calculations with and without solid-state diffusion, between $k(f_s)$ and k_e, and between the solidification interval as calculated for the experimental data and for the theoretical and experimental Scheil-Gulliver cases, respectively. Table 2 shows the average values of $k(f_s)$ and k_e. Before the differences between theoretical Scheil-Gulliver calculations and STEM-EDS measurements are presented, the relevance of the experimental data points and the validity of the data processing

scheme have to be discussed. First, the extent of solid-state diffusion must be assessed due to its potentially strong effect on the reconstructed composition profiles. Comparison between the Scheil-Gulliver calculations with and without solid-state diffusion shows that diffusion is limited to the intercellular region, while the inner composition of the cell remains little affected. This is related to the solidification cell size of the studied material. The heat treatment of 1 seconds for 1000°C being an unrealistically large overestimation of the *in-situ* heat treatment, it is safe to assume that solid-state diffusion had a limited effect on the composition profile, even when considering a much faster diffusion along the intracellular dislocations. Furthermore, while the presence of nano-oxides observed in the intercellular regions implies a local depletion in some chemical elements, they are assumed to have a negligible effect on the redistribution profile. Therefore, the variations in chemical composition as measured by STEM-EDX are mostly due to segregation during solidification, while others phenomena such as diffusion and precipitation appear to have a negligible effect. Second, the validity of the modified WIRS method has to be discussed. The reconstructed segregation profiles for Mn and Mo in Figure 2 follow trends that do not depend on the measurement area, despite the large relative variations observed between the areas (Table 1). This is also true in the case of Si which, despite being excluded from the data processing, shows a noisy but clear redistribution behavior. Furthermore, the measurements of all three areas are homogeneously distributed along the segregation profile, such that the average solid fractions corresponding to areas 1, 2 and 3 are 0.53, 0.48 and 0.49, respectively. Finally, there is a very good agreement in the solidification interval corresponding to the experimental Scheil-Gulliver and to the STEM-EDS measurements in Figure 4. This shows that the modified WIRS method is able to reconstruct segregation profiles, and thus solidification interval, using datasets which average concentration slightly differs from the nominal composition. The proposed method is thus a powerful tool for the experimental determination of the segregation behavior of minor elements since their EDS quantifications are prone to experimental uncertainties.

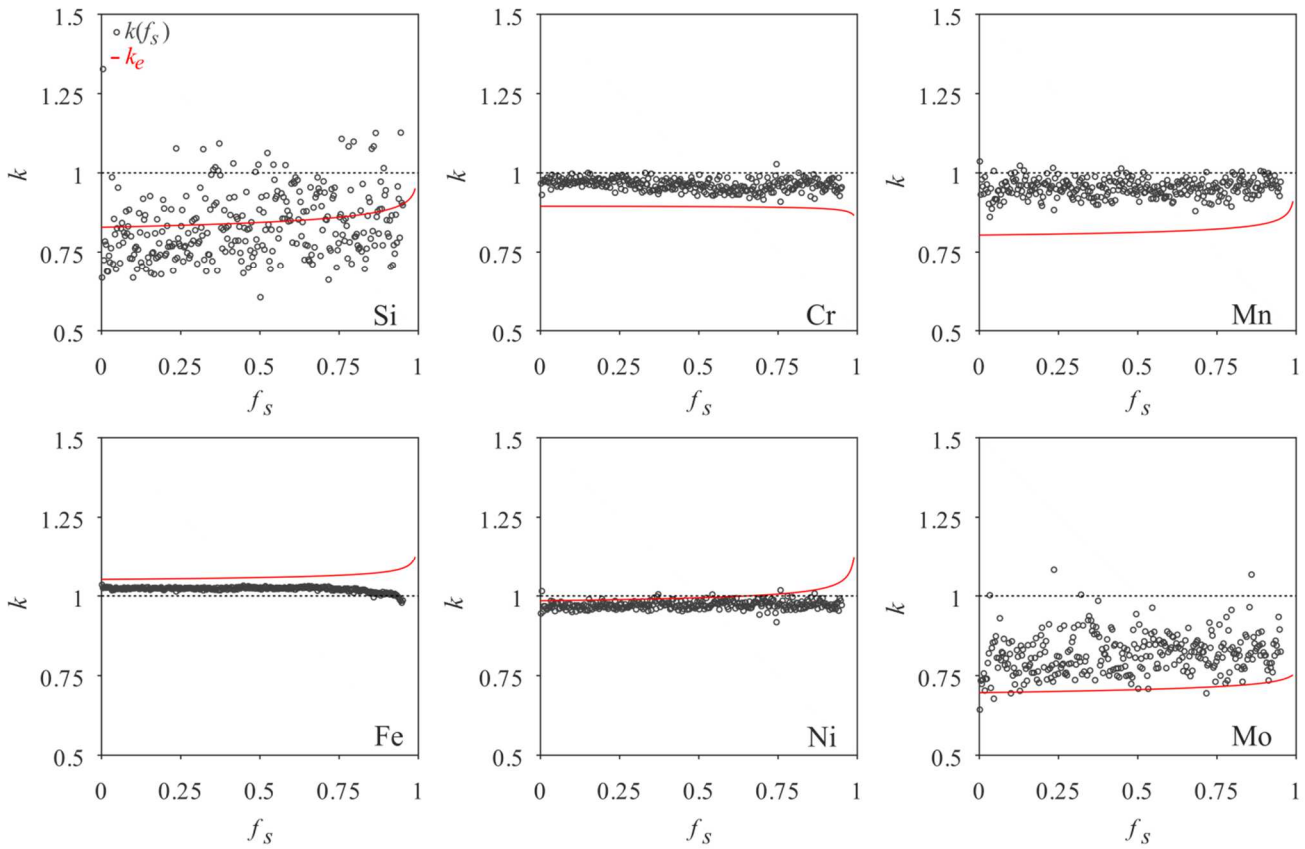

Figure 3: *Comparison between coefficients k_e and $k(f_s)$*

	Si	Cr	Mn	Fe	Ni	Mo
k_e	0.84	0.89	0.81	1.06	0.99	0.71
k	0.83	0.96	0.95	1.02	0.97	0.82

Table 2*: Comparison between the mean values of k (for f_s up to 0.95) and of k_e (for f_s up to 0.75).*

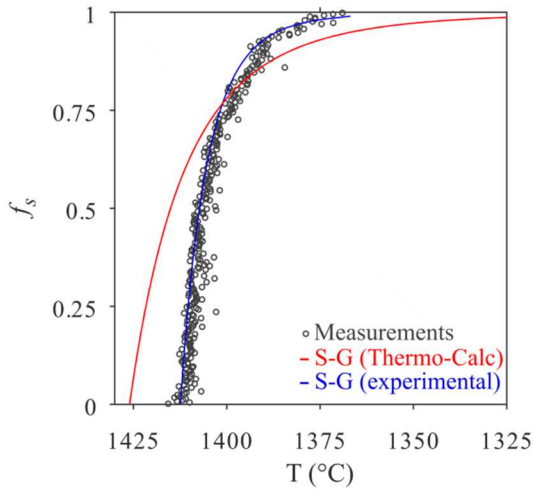

Figure 4: *Evolution of the solid fraction as a function of the temperature for Scheil-Gulliver calculations and experimental data. Solidification temperatures correspond to the equilibrium.*

A general good agreement is found between experimental measurements and Thermo-Calc calculations, with experimental segregation profiles of similar or lower magnitudes compared to the calculated ones (Figure 1). This implies that k is always similar or slightly closer to 1 than k_e (Figure 2 and Table 2), and that the 95% solidification interval $\Delta T_{0.95}$ is narrower for the experimental data compared to the calculations, respectively 30 °C and 60 °C (Figure 3). The small differences observed between Scheil-Gulliver simulations and the experimental measurements likely arise from the relatively fast solidification rates involved in this study, which can as fast as the scanning speed [21], i.e. 30 mm/s. The partition coefficient k is known to tend towards 1 when the solidification rate increases owing to the competition between the interface speed and the diffusion speed [22]. As a mean of comparison, phase field simulations performed for a solidification rate of 25 mm/s yielded an extent of segregation in Nb 2.5 times lower than classical Scheil-Gulliver equations for a nickel-base alloy [23]. Such considerations agree well with the general trend, although seemingly significant differences between k and k_e can result in very similar redistribution profiles (see for instance Mo).

To conclude, STEM-EDS measurements processed by the modified WIRS method are shown to be a powerful tool for the experimental determination of chemical heterogeneities arising from the additive manufacturing process. The proposed modification of the WIRS method partially negates the experimental uncertainty, especially for minor elements. Scheil-Gulliver simulations give a good first approximation of the evolution of local chemistry and of the equilibrium solidification interval during solidification of an additively manufactured 316L using slow solidification rates. While not directly applicable to conventional L-PBF parts, this means that Scheil-Gulliver calculations are sufficient to predict the solute redistribution behavior during Laser Metal Deposition (LMD), where scanning rates typically range between 2.5 and 25 mm/s. Further work is ongoing to investigate the effect of faster solidification rates, more representative of the L-PBF process, on the solute redistribution during solidification.

Funding: This research did not receive any specific grant from funding agencies in the public, commercial, or not-for-profit sectors.

References

[1] W.M. Tucho, P. Cuvillier, A. Sjolyst-Kverneland, V. Hansen, Mater. Sci. Eng. A 689 (2017) 220–232.

[2] Y.M. Wang, T. Voisin, J.T. McKeown, J. Ye, N.P. Calta, Z. Li, Z. Zeng, Y. Zhang, W. Chen, T.T. Roehling, R.T. Ott, M.K. Santala, P.J. Depond, M.J. Matthews, A. V. Hamza, T. Zhu, Nat. Mater. 17 (2018) 63–71.

[3] J.R. Trelewicz, G.P. Halada, O.K. Donaldson, G. Manogharan, JOM 68 (2016) 850–859.

[4] Y. Zhong, L. Liu, S. Wikman, D. Cui, Z. Shen, J. Nucl. Mater. 470 (2016) 170–178.

[5] H. Xiao, S. Li, X. Han, J. Mazumder, L. Song, Mater. Des. 122 (2017) 330–339.

[6] J. Krell, A. Röttger, K. Geenen, W. Theisen, J. Mater. Process. Technol. 255 (2018) 679–688.

[7] E. Jägle, Z. Sheng, P. Kürnsteiner, S. Ocylok, A. Weisheit, D. Raabe, Materials (Basel). 10 (2016) 8.

[8] D. Grange, J.D. Bartout, B. Macquaire, C. Colin, Materialia 12 (2020) 100686.

[9] X.P. Li, X.J. Wang, M. Saunders, A. Suvorova, L.C. Zhang, Y.J. Liu, M.H. Fang, Z.H. Huang, T.B. Sercombe, Acta Mater. 95 (2015) 74–82.

[10] B. AlMangour, Y.K. Kim, D. Grzesiak, K.A. Lee, Compos. Part B Eng. 156 (2019) 51–63.

[11] S. Gorsse, C. Hutchinson, M. Gouné, R. Banerjee, Sci. Technol. Adv. Mater. 18 (2017) 584–610.

[12] U. Scipioni Bertoli, B.E. MacDonald, J.M. Schoenung, Mater. Sci. Eng. A 739 (2019) 109–117.

[13] G. Mohr, S.J. Altenburg, K. Hilgenberg, Addit. Manuf. 32 (2020) 101080.

[14] K.M. Bertsch, G. Meric de Bellefon, B. Kuehl, D.J. Thoma, Acta Mater. 199 (2020) 19–33.

[15] S.-H. Sun, T. Ishimoto, K. Hagihara, Y. Tsutsumi, T. Hanawa, T. Nakano, Scr. Mater. 159 (2019) 89–93.

[16] O. Andreau, I. Koutiri, P. Peyre, J.D. Penot, N. Saintier, E. Pessard, T. De Terris, C. Dupuy, T. Baudin, J. Mater. Process. Technol. 264 (2019) 21–31.

[17] S. Katayama, A. Matsunawa, in: Int. Congr. Appl. Lasers Electro-Optics, Laser Institute of America, 1984, pp. 60–67.

[18] P. Deng, M. Karadge, R.B. Rebak, V.K. Gupta, B.C. Prorok, X. Lou, Addit. Manuf. 35 (2020) 101334.

[19] M. Ganesan, D. Dye, P.D. Lee, Metall. Mater. Trans. A Phys. Metall. Mater. Sci. 36 (2005) 2191–2204.

[20] C.J. Farnin, S. Orzolek, J.N. DuPont, Metall. Mater. Trans. A Phys. Metall. Mater. Sci. 51 (2020) 5771–5780.

[21] R. Shi, S.A. Khairallah, T.T. Roehling, T.W. Heo, J.T. McKeown, M.J. Matthews, Acta Mater. 184 (2020) 284–305.

[22] M.J. Aziz, T. Kaplan, Acta Metall. 36 (1988) 2335–2347.

[23] T. Keller, G. Lindwall, S. Ghosh, L. Ma, B.M. Lane, F. Zhang, U.R. Kattner, E.A. Lass, J.C. Heigel, Y. Idell, M.E. Williams, A.J. Allen, J.E. Guyer, L.E. Levine, Acta Mater. 139 (2017) 244–253.